Temperature-dependent thermal and thermoelectric properties of n-type and p-type Sc_{1−x}Mg_{x}N

Bivas Saha, Jaime Andres Perez-Taborda, Je-Hyeong Bahk, Yee Rui Koh, Ali Shakouri, Marisol Martin-Gonzalez, and Timothy D. Sands

Phys. Rev. B **97**, 085301 — Published 1 February 2018

DOI: 10.1103/PhysRevB.97.085301

Temperature Dependent Thermal and Thermoelectric Properties of *n*-type and *p*-type $Sc_{1-x}Mg_xN$

Bivas Saha[1], Jaime Andres Perez-Taborda[2], Je-Hyeong Bahk[3], Yee Rui Koh[4], Ali Shakouri[4], Marisol Martin-Gonzalez[2] and Timothy D. Sands[5]

[1]*Department of Materials Science and Engineering, University of California, Berkeley, CA 94720, USA.*
[2]*Instituto de Microelectrónica de Madrid, CSIC, C/ Isaac Newton 8, Tres Cantos, 28760 Madrid, Spain.*
[3]*Department of Mechanical and Materials Engineering, University of Cincinnati, Cincinnati, OH 45221, USA.*
[4]*School of Electrical Engineering and Computer Engineering, Purdue University, West Lafayette, IN-47907, USA.*
[5]*Bradley Department of Electrical and Computer Engineering and Department of Materials Science and Engineering, Virginia Tech, Blacksburg, VA 24061, USA.*

Scandium Nitride (ScN) is an emerging rocksalt semiconductor with octahedral coordination, and an indirect bandgap. ScN has attracted significant attention in recent years for its potential thermoelectric applications, as a component material in epitaxial metal/semiconductor superlattices, and as a substrate for defect-free GaN growth. Sputter-deposited ScN thin films are highly degenerate *n*-type semiconductors, and exhibit a large thermoelectric power factor of ~3.5 $\times 10^{-3}$ W/m-K^2 at 600K-800K. Since practical thermoelectric devices require both *n*- and *p*-type materials with high thermoelectric *figures-of-merit*, development and demonstration of highly efficient *p*-type ScN is extremely important. Recently, the authors have demonstrated *p*-type $Sc_{1-x}Mg_xN$ thin film alloys with low Mg_xN_y mole-fractions within the ScN matrix. In this article, we demonstrate temperature dependent thermal and thermoelectric transport properties, including large thermoelectric power factors in both *n*- and *p*-type $Sc_{1-x}Mg_xN$ thin film alloys at high temperatures (up to 850K). Employing a combination of temperature dependent Seebeck coefficient, electrical conductivity and thermal conductivity measurements, as well as detailed Boltzmann transport based modeling analyses of the transport properties, we demonstrate that *p*-type $Sc_{1-x}Mg_xN$ thin film alloys exhibit a maximum thermoelectric power factor of ~0.8 $\times 10^{-3}$ W/m-K^2 at 850K. The thermoelectric properties are tunable by adjusting the Mg_xN_y mole-fraction inside the ScN matrix, thereby shifting the Fermi energy in the alloy films from inside the conduction band in case of undoped *n*-type ScN to inside the valence band in highly hole-doped *p*-type $Sc_{1-x}Mg_xN$ thin film alloys. The thermal conductivities of both the *n*- and *p*-type films were found to be undesirably large for thermoelectric applications. Thus, future work should address strategies to reduce the thermal conductivity of $Sc_{1-x}Mg_xN$ thin-film alloys, without affecting the power factor for improved thermoelectric performance.

Correspondence should be sent to Bivas Saha (bsaha@berkeley.edu)

I. INTRODUCTION

Thermoelectric materials convert waste heat energy directly into electrical power and are attractive for harvesting energy in automobiles, power plants, and for deep space exploration[1-3]. Such materials could also be used as a Peltier cooler in microelectronic chips and devices, where unwarranted heat generation (hot spots in integrated circuits (IC)) limit device efficiencies[4-5]. Devices made from thermoelectric elements are environmentally friendly and do not have any movable parts except for a fan in most cases.

The efficiency of a thermoelectric material is represented by its dimensionless *figure-of-merit,* $ZT = \frac{S^2\sigma T}{\kappa_e+\kappa_p}$, where S is the Seebeck coefficient, σ is the electrical conductivity, κ_e and κ_p are the electronic and lattice contributions to the thermal conductivity respectively, and T is the absolute temperature. The higher the thermoelectric *figure-of-merit (ZT)* of a material, the more efficient the energy conversion is. The numerator $S^2\sigma$, or S^2/ρ with resistivity ρ, is called the power factor and is determined by charge carrier transport. To be competitive with conventional power-generator and refrigeration technology, thermoelectric materials need to exhibit a *ZT* of about 3-4 over a wide temperature range. However, extensive research in the last decade has only improved the *ZT* to ~2 at high operating temperatures[6-8]. Designing high efficiency thermoelectric materials having *ZT >2* is particularly challenging due to the mutually conflicting design parameters. While individual thermoelectric materials must exhibit high *ZT* values at the required temperature ranges of interest, practical thermoelectric devices require both *n*-type (electron conducting) and *p*-type (hole-conducting) materials with high *ZTs*, as well as effective methods to integrate them with metals having low contact resistances. Such restrictions naturally impose additional challenges in terms of material selection and device fabrication techniques.

Scandium Nitride (ScN) is a promising group III(B)-nitride rocksalt semiconductor with an indirect bandgap[9-15] and octahedral coordination. ScN has attracted significant interest in recent days for its potential applications in thermoelectricity[16-18], as a semiconducting component material in epitaxial single crystalline nitride metal/semiconductor superlattices[19-22] for their eventual thermoelectric applications, and for other solid-state device applications such as substrates for the growth of high-quality GaN-based devices[23], as well as for reducing dislocation densities in GaN[24]. Like most other transition metal nitrides (TMNs), ScN is structurally and chemically stable, mechanically hard (23 GPa), corrosion resistant, and possesses high melting temperatures in excess of 2873K[25]. Due to its rocksalt (cubic) crystal structure, ScN also offers a materials platform for engineering the band structure of alloys with the III-V nitride semiconductors (AlN, GaN, and InN, which adopt the wurtzite crystal structure without ScN) for applications where integration of the semiconductor with cubic (rocksalt) metals is required[26]. Although controversies persisted about the nature of its electronic structure during the 1990's and early 2000s, recent experimental results[10,27] and theoretical modeling[9,28] have demonstrated conclusively that ScN has an indirect bandgap of 0.9-1.2 eV and a direct gap of 2.2 eV. ScN and its rocksalt solid solution $Al_xSc_{1-x}N$ have been developed and utilized in recent years to grow the first epitaxial metal/semiconductor multilayers and superlattices based on (Hf,Zr)N/ScN[19-22] and TiN/(Al,Sc)N[29,30] material systems. Wurtzite $Al_xSc_{1-x}N$ has also attracted interest for its large piezoelectric respons[31]. In short, ScN is an emerging III-V nitride semiconductor for future applications and deserves attention to harnessing its potential for real practical devices.

Kerdsongpanya et al[17] have demonstrated an extremely large power factor of 2.5×10^{-3} W/m-K^2 in ScN thin films grown on Al_2O_3 substrates, which was anomalously high for common transition metal nitrides. Later research by *Burmistrova et al.*[16] have improved the power factor values to ~ (3.3-3.5) $\times 10^{-3}$ W/m-K^2 at 600-850K in sputter-deposited *n*-type ScN thin films grown on MgO substrates. These power factors at 600-850K temperature ranges are higher than those of Bi_2Te_3 and its alloys at 400 K[2,8], as well as the best high-temperature thermoelectric materials such as La_3Te_4[32] at 600 K, and compare well with undoped crystalline SiGe[33] in the same temperature range. The origin of such large power factors can be explained by the changes in ScN's electronic structure with respect to the presence of point defects and impurities (such as Sc and N vacancies[34], and doping effects of O and C on N-sites, and Ca and Ti on Sc sites on ScN's electronic structure[35]). For sputter-deposited ScN grown on MgO substrate (deposited with the same sputtering machine albeit with a slightly different growth condition than the films grown in this study), *Burmistrova et al.*[16] have showed that as-deposited ScN thin films exhibit a large *n*-type carrier concentration of (1-6) $\times 10^{20}$ cm^{-3} due to the presence of oxygen as unwanted dopant impurities incorporated during deposition. Several other studies have also reported the presence of carbon (C) and fluorine (F) as impurities inside sputter-deposited ScN thin films[17,36], which could potentially be electronically active. However, the ScN and $Sc_{1-x}Mn_xN$ thin film alloys studied here are not expected to exhibit significant concentrations of these impurities based on *Burmistrova et al's* measurements of samples grown in the same deposition system[16]. Coupled with a high electrical mobility of ~100 cm^2/Vs at room temperature, the ~3×10^{20} cm^{-3} carrier concentration in ScN created favorable conditions for high thermoelectric power factors, with the measured Seebeck coefficient of -156μV/K, and an electrical conductivity of ~1300 S/cm at 840 K[16]. While the large power factor in the as-deposited *n*-type ScN is attractive for thermoelectricity, practical devices also require a highly efficient *p*-type material. Reducing the carrier concentration in ScN, and eventually turning it into a *p*-type semiconductor was also important for a host of other applications. For example, in epitaxial single crystalline metal/semiconductor superlattices, the semiconducting materials are required to have low carrier concentrations in order to favor thermionic emission over barriers rather than tunneling or thermionic-field emission through barriers. Likewise, for several other electronic and optoelectronic applications such as in *p-n* junctions, light emitting diodes (LED) and solar cells, ScN requires low and controlled carrier concentrations in the *n*-type regime as well as *p*-type ScN, typically with high hole-concentrations.

With that motivation, the authors have previously demonstrated *p*-type $Sc_{1-x}Mn_xN$ thin film alloys[10] and $Sc_{1-x}Mg_xN$ thin film alloys[37] more recently by solid-state alloying of ScN with Mn_xN_y and Mg_xN_y, respectively. A detailed description of growth, microstructural characterization, room temperature optical, and temperature-dependent electrical properties such as mobility and carrier concentration, are presented in Ref. 37. The results can be summarized as follows: the *p*-type $Sc_xMg_{1-x}N$ thin film alloys (a) were substitutional solid solutions without any detectable Mg_xN_y precipitation, phase segregation, or secondary phase formation; (b) exhibited a maximum hole-concentration of 2.2×10^{20} cm^{-3} and hole mobility of 21 cm^2/Vs; (c) didn't show any defect states inside the direct gap of ScN, thus retaining its basic electronic structure; and (d) exhibited impurity scattering by Mg addition that dominated hole conduction at high temperatures. In this article, we describe the temperature dependent thermal and thermoelectric properties of *n*-type and *p*-type $Sc_xMg_{1-x}N$ thin film alloys across the carrier type transition

range. Boltzmann transport based modeling analyses were also performed to explain the transport properties in light of the electronic structure of the materials.

II. METHODS

1. Growth: $Sc_{1-x}Mg_xN$ thin films were grown on [001] MgO substrates with a reactive dc-magnetron co-sputtering technique inside a load-locked turbomolecular pumped high vacuum deposition system with a base pressure of ~10^{-8} torr (PVD Products, Inc.). The growth chamber had the capability to accommodate four targets and was equipped with three dc power supplies. The Sc (99.998% purity), and Mg (99.99%) targets had dimensions of 2 in. diameter and 0.25 in. thickness. All depositions were performed with an Ar/N_2 mixture having 6 sccm of N_2 and 4 sccm of Ar at a deposition pressure of 5 mTor. The targets were sputtered in constant power mode. The substrates were maintained at 750°C during deposition, as determined using an infrared pyrometer operated in the wavelength range of 0.8–1.1 μm, together with a thermocouple.

2. Seebeck Coefficient and Electrical Resistivity Measurement: In-plane electrical resistivity (ρ) and the Seebeck coefficient (S) were simultaneously measured on a commercial Linseis LSR-3 system. The Seebeck coefficient and electrical conductivity from 300 - 850 K were measured on a commercial Linseis LSR-3 system using a differential voltage/temperature technique. The accuracy of the system is ±5%. This equipment is periodically calibrated to assure metrology. The value of power factor has been calculated by: $PF = \frac{S^2}{\rho}$.

Additionally, the electrical resistivity (ρ), carrier concentration (n) and mobility (μ) of the samples were measured by Hall effect measurements from room temperature until 850 K using the four Au-coated point van der Pauw method. The measurements were performed using an Ecopia HMS-5000 Hall Effect Measurement System, with fixed magneto-flux density of 0.55T +/-0.03 Tesla. This system is also calibrated periodically.

4. Thermal Conductivity Measurement: We employed the time-domain thermoreflectance[38-39] (TDTR) to measure the thermal conductivity of the $Sc_{1-x}Mg_xN$ thin film alloys. TDTR is a non-destructive optical pump-probe method to measure thermal conductivity. A Ti: Sapphire laser was used in the TDTR setup to create short pulsed laser beams with ~12.5ns repetition rate. In the measurement, the laser pulses were split into a pump beam and probe beam. The pump beam is used to create a temperature rise on the sample surface. In considering the thickness constraint of the samples (~240nm), we modulated the pump beam at a frequency of 6-10MHz. The pump modulation frequency (f) is inversely proportional to the heat penetration depth (d) with the relation of $d = \sqrt{\frac{k}{\Pi C_p f}}$, where k and C_p are the thermal conductivity and heat capacity of the film respectively. The radii of the laser beam are around 5.5-6.0μm at the sample surface. A 70nm aluminum transducer was coated on the sample to absorb the incident beam. The probe laser is relative low in laser power to probe the change of thermoreflectance on the sample surfaces. A Si-photodetector and RF lock-in amplifier are used to collect the reflected probe beam signal. The probe beam signal was fitted with a 3D thermal diffusion model based on thermal quadrupoles. Interface resistance between Al transducer and $Sc_{1-x}Mg_xN$ thin film alloys

was included in the model. In order to observe the thermal conductivity in the different ambient temperature, a Linkam THMS600 temperature stage is used. A precise temperature resolution 0.1^{o}C was achieved by using the Linkam THMS600 stage.

3. Electron transport modeling for *n*-type and *p*-type ScN: ScN is an indirect bandgap semiconductor with an indirect band gap of 0.89 eV between Γ and X valleys [Re. 28]. We fixed the band gap value for our electron transport modeling in the entire temperature and carrier concentration ranges. The conduction band is particularly asymmetric, which is modeled as two effective masses, longitudinal and transverse of $m_l^* = 2.06m_0$ and $m_l^* = 0.28m_0$, respectively. The hole effective mass used in the modeling is $m_h^* = 0.60m_0$. Both bands have high non-parabolicity α = ~ 1 eV^{-1} in the non-parabolic dispersion given by $E(1+\alpha E) = (\hbar k)^2/2m^*$.

Our transport model is based on the linearized Boltzmann transport equation (BTE) with an approximate relaxation time. All of the transport properties are expressed as integral functions of the differential conductivity $\sigma_d(E)$ over energy E, defined as[Ref. 41]

$$\sigma_d(E) = e^2\tau(E)v_x^2(E)\rho_{DOS}(E)\left(-\frac{\partial f_0(E)}{\partial E}\right), \quad (1)$$

where e is the electron charge, τ is the relaxation time, ρ_{DOS} is the density of states, v is the carrier velocity and f_0 is the Fermi-Dirac distribution. For the multiple-band transports in ScN, the transport properties are calculated in each of the bands with the relative position of the Fermi level E_F from the band extremum and the contributions from each band are then added together to find the total transport values in the bulk. The electrical conductivity σ and the Seebeck coefficient S are given, respectively, by

$$\sigma = \sum \int \sigma_d(E)dE, \quad (2)$$

$$S = \sum\left(\frac{k_B}{q}\right)\int\left[\frac{(E-E_F)}{k_BT}\right]\frac{\sigma_d(E)}{\sigma}dE\ , \quad (3)$$

where Σ is the sum over the bands, q is $-e$ for the conduction bands and $+e$ for the valence bands, T is the absolute temperature, and E_F is the Fermi energy. The electrical resistivity ρ is the reciprocal of the electrical conductivity such that $\rho=1/\sigma$. Once the electrical conductivity and Seebeck coefficients are measured experimentally, they are curve-fitted simultaneously using Eq. (2)-(3) with the Fermi level as the adjustable parameters. Some other parameters regarding the electron scattering are also adjusted to finely tune the fitting results.

III. STRUCTURAL CHARACTERIZATION

Characteristic X-ray diffraction (XRD) spectra of *n*-type undoped-ScN, *n*-type $Sc_{1-x}Mg_xN$, and *p*-type $Sc_{1-x}Mg_xN$ thin film alloy (presented in Ref. 37) showed that the films grow with 002 orientations on [001] MgO substrates. The full-width-at-half-maxima (FWHM) of the rocking curves (ω-scan) were between 0.6°-0.8° for all films, suggestive of nominally single crystalline epitaxial growth. XRD measurements also show that the lattice constant of the undoped-ScN

film was 4.50Å, consistent with literature reports[9-12]; while incorporation of Mg_xN_y within the ScN matrix did not change the lattice constant appreciably. The reciprocal space X-ray maps (RSM) clearly demonstrated (see Ref. 37) that the film and the substrate diffraction peaks were separated along the horizontal (Q_x) axis indicating strain relaxed thin film growth. Such strain relaxation was not

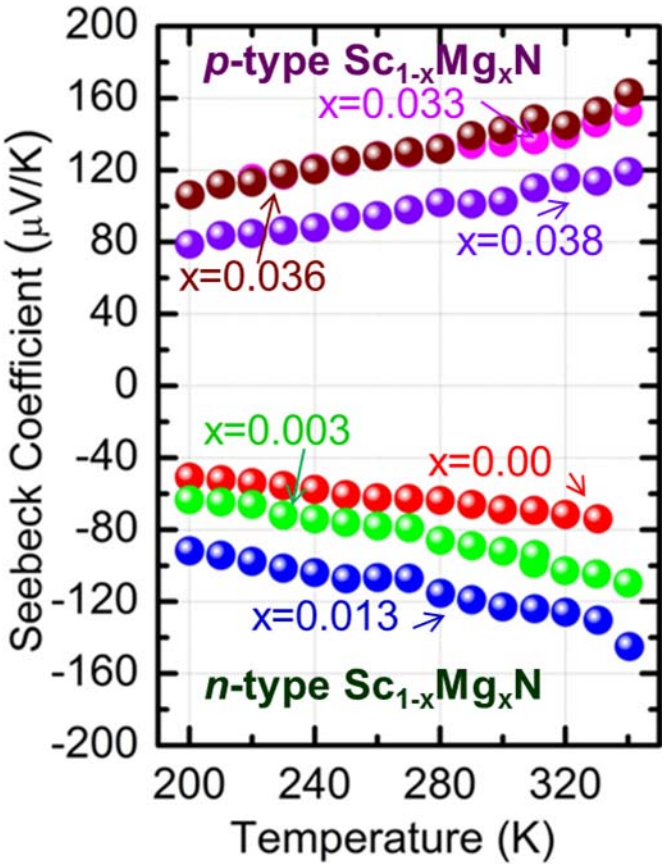

Figure 1. Low-temperature Seebeck coefficients of three n-type and three p-type $Sc_{1-x}Mg_xN$ thin filmalloys are presented. All of the alloys show an increase in the magnitude of the Seebeck coefficient with increasing temperature. The Seebeck coefficient values increase slightly with increasing Mg_xN_y concentration inside the ScN matrix for the n-type samples. For the p-type films, the Seebeck coefficient decreases slightly with increasing hole concentrations as would be expected.

surprising given the ~7% lattice mismatch between the $Sc_{1-x}Mg_xN$ thin film alloys and the MgO substrates. High-resolution transmission electron microscopy (HREM) along with a high-angle annular dark field scanning transmission electron microscopy (HAADF-STEM) images clearly showed edge dislocations due to the strain relaxation. The substrate (MgO) and film ($Sc_{0.97}Mg_{0.03}N$) interface was atomically sharp and abrupt, while distinct and clear lattice fringes from the film and the substrate were clearly visible in the microscopy image. No signature of any Mg_xN_y precipitation inside ScN matrix, or secondary phase formations was observed within the studied composition range. Since the $Sc_{1-x}Mg_xN$ thin films were grown on MgO substrates, traditional composition analysis techniques where the probe beams are directed normal to the surface (such as Rutherford Backscattering Spectrometry (RBS)) were not suitable to separate the Mg signals from the film and the substrate. Therefore, HRTEM-Energy Dispersive X-ray

spectroscopy (EDS) was employed for compositional analysis of a film, and the results were subsequently used to benchmark the composition of other films studied in this work by interpolation using Mg target sputter power. The thickness of the films were kept constant at ~400 nm.

IV. TEMPERATURE DEPENDENT SEEBECK COEFFICIENT AND ELECTRICAL RESISTIVITY

Since an explanation of the thermoelectric properties requires the knowledge of variations in room-temperature resistivity and carrier concentrations across the compositional range, readers are referred to Fig. 3 in Ref. 37, where the resistivity and carrier concentrations results are shown as a function of Mg_xN_y concentration inside the ScN matrix. It is clear from the figure that incorporation of Mg_xN_y inside the ScN matrix acts as an efficient hole dopant, and reduces the electron concentration from undoped ScN. The resistivity of undoped ScN was 0.4 mΩ-cm and increased to ~10^4 mΩ-cm with increasing Mg_xN_y concentration before the films exhibited *p*-type conduction. Similarly, the *n*-type carrier concentration decreased from 7×10^{20} cm^{-3} for undoped-ScN, to 2×10^{18} cm^{-3} for the $Sc_{0.975}Mg_{0.025}N$ (x=0.025) thin film alloys before the carrier type transition. The resistivity of the *p*-type $Sc_{1-x}Mg_xN$ thin film alloys decreased with further increase in Mg_xN_y concentrations inside the ScN matrix, primarily due to the increase in hole-concentration. As highly efficient thermoelectric materials require high electrical conductivity and moderate carrier concentrations for sufficiently high Seebeck coefficients, we focused on three *n*-type and three *p*-type samples for temperature-dependent thermoelectric property analysis.

The magnitudes of the low-temperature (200K-340K) Seebeck coefficients of all the six samples increased linearly with increasing temperature (see Fig. 1). The *n*-type undoped ScN exhibited a Seebeck coefficient of -58 μV/K at 200 K, which increased in magnitude to -78 μV/K at 340 K. Similarly, the highly conductive *p*-type $Sc_{0.962}Mg_{0.038}N$ (x=0.038) alloy film demonstrated a Seebeck coefficient increase from 80 μV/K to 120 μV/K with a corresponding increase in temperature from 200 K to 340 K. It is interesting to note that the Seebeck coefficients of the *n*-type $Sc_{0.997}Mg_{0.003}N$ and $Sc_{0.987}Mg_{0.013}N$ alloy films were slightly higher than that of the undoped ScN thin-film, increasing from -63 μV/K at 200 K to -110 μV/K at 340 K for the $Sc_{0.997}Mg_{0.003}N$ alloy film, and from -90 μV/K at 200 K to -145 μV/K at 340 K for the $Sc_{0.987}Mg_{0.013}N$ alloy film. Since the room temperature resistivity of the *n*-type $Sc_{0.997}Mg_{0.003}N$ and $Sc_{0.987}Mg_{0.013}N$ alloy films were a factor of 666× and 3333× larger compared to undoped-ScN respectively, such small increases in the Seebeck coefficient could be due to the significant reduction of electron mobility with relatively small carrier concentration reduction. The Seebeck coefficients of *p*-type $Sc_{0.967}Mg_{0.033}N$ and $Sc_{0.964}Mg_{0.036}N$ alloy films were very similar to each other over the entire temperature range, even though the *p*-type $Sc_{0.967}Mg_{0.033}N$ alloy film exhibited ~10 times larger resistivity near room temperature in comparison to that of the *p*-type $Sc_{0.964}Mg_{0.036}N$ alloy.

Temperature dependent Seebeck coefficient, electrical resistivity, and power factors of *n*-type undoped-ScN and *p*-type $Sc_{0.962}Mg_{0.038}N$ thin film alloy in the 300 ~ 850 K temperature range are presented in Fig. 2(a, b, and c respectively) with both the heating and cooling cycles. The heating and cooling curves are extremely close to each other demonstrating low experimental variations over high-temperature thermal cycles, except for the Seebeck coefficient

measurements for *p*-type $Sc_{0.962}Mg_{0.038}N$ thin film alloy, where small deviations were observed (details presented in the SM section). The Seebeck coefficient of undoped ScN increased by a factor of ~3× from 300 K to 850 K, which is consistent with *Burmistrova et al's.*[16] previous reports on the thermoelectric properties of undoped ScN thin film. In contrast to the undoped ScN film, the Seebeck coefficient of the *p*-type $Sc_{0.962}Mg_{0.038}N$ thin film alloy increased by a factor of ~5× over the same temperature range. A maximum Seebeck coefficient of 240 μV/K was achieved for the *p*-type $Sc_{0.962}Mg_{0.038}N$ thin film alloy film at ~800K, which is significantly larger in magnitude than the maximum Seebeck coefficient of -150 μV/K for undoped ScN in the same temperature range. Since traditionally superior thermoelectric materials[2,3] like Bi_2Te_3, PbTe and more recently SnSe[6] exhibit magnitudes of Seebeck coefficients in the 150 to 400 μV/K range at high temperatures, the high Seebeck coefficients of *n*-type undoped ScN and *p*-type $Sc_{0.962}Mg_{0.038}N$ thin film alloy are extremely encouraging.

The electrical resistivity of the undoped ScN thin film increased from 0.3 mΩ-cm to 0.9 mΩ-cm with increasing temperature from 300 K to 850 K. Such an increase in resistivity as a function of

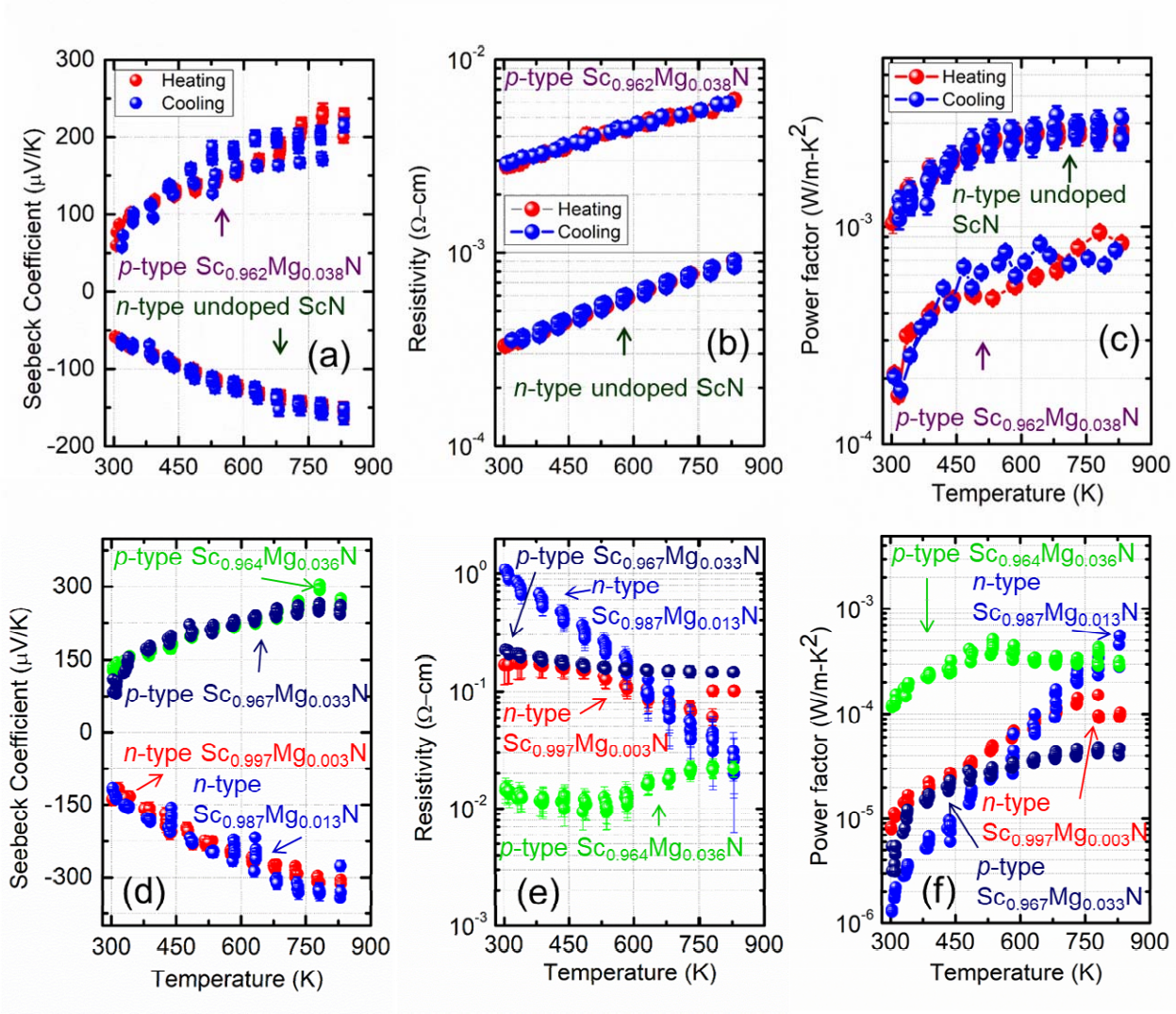

Figure 2: Seebeck coefficient (a), electrical resistivity (b), and power factors (c) of n-type undoped ScN and p-type $Sc_{0.962}Mg_{0.038}N$ thin film alloy are presented for both heating and cooling cycles. Seebeck coefficient of both the thin films increases with increasing temperature albeit with different factors. The resistivity of the n-type undoped ScN increases by ~3 times, while the resistivity of the p-type $Sc_{0.962}Mg_{0.038}N$ thin film alloy remains relatively unchanged. Figure (c) show that the n-type undoped ScN exhibits a maximum power factor of 3×10^{-3} W/m-K^2, while the p-type $Sc_{0.962}Mg_{0.038}N$ thin film alloy hass a maximum power factor of 0.8×10^{-3} W/m-K^2 at high temperature. Heating cycles of Seebeck coefficient (d), electrical resistivity (e), and power factors (f) of two other n-type and p-type samples are also presented. While the Seebeck coefficients of all four samples increase with increasing temperatures, the variations in resistivity are different for different samples; and their overall power factors are smaller.

temperature is reminiscent of metallic conduction with the Fermi energy within the bands. Indeed, the electron transport modeling analysis will show (below) that the Fermi level of undoped-ScN lies ~0.12 eV above the band-edge inside the conduction band. The resistivity of *p*-type $Sc_{0.962}Mg_{0.038}N$ thin film alloy (having the smallest resistivity among the *p*-type films) increases similar to the case for *n*-type undoped ScN over the entire temperature range. (See Fig. 2(b)) The resistivity is also a factor of ~10× larger in the *p*-type $Sc_{1-x}Mg_xN$ thin film alloy compared to the undoped ScN. The increase in resistivity was due to the decrease in mobility and carrier concentrations, as a result of Mg_xN_y incorporation inside the ScN matrix as also seen in Ref. 37.

Having measured the Seebeck coefficient and electrical resistivity as a function of temperature, the thermoelectric power factors ($\frac{S^2}{\rho}$) were calculated, and presented in Fig. 2(c). Undoped-ScN exhibits a thermoelectric power factor of 3×10^{-3} W/m-K^2 in the 600K-850K temperature range. Such a large power factor is consistent with *Burmistrova et al's.*[16] previous reports on undoped ScN, and is one of the highest reported[40] power factors for any material in the given temperature range. Among the III-V semiconducting materials, ScN demonstrated the best power factors thus far, and only some complex thermoelectric materials such as[40] $Ba_{0.1}La_{0.05}Yb_{0.07}Co_4Sb_{12}$, $(Si_{80}Ge_{20})_{80}(Si_{100}P_3)_{20}$ exhibit power factors greater than that of undoped ScN. Similarly the *p*-type $Sc_{1-x}Mg_xN$ thin film alloy exhibited a maximum power factor of $(0.8\text{-}0.9) \times 10^{-3}$ W/m-K^2 in the 600K-850K temperature range, which is a factor of ~3-4× smaller than that of undoped-ScN in the same temperature range. This lower power factor is due to the higher resistivity of the *p*-type alloy film with respect to the undoped ScN, overcoming the enhancement associated with the increased Seebeck coefficient. The power factor of the *p*-type $Sc_{0.962}Mg_{0.038}N$ thin film alloy nevertheless has one of the largest values reported[40] in the literature for *p*-type materials thus far, and is consistent with the fact that the *p*-type materials usually exhibit smaller power factors compared to their *n*-type counterparts. Careful search showed that only complex *p*-type materials like $(Si_{80}Ge_{20})_{70}(Si_{100}B_5)_{30}$, PbTeSe, and others exhibit power factor higher than 0.8×10^{-3} W/m-K^2 over the 600K-850K temperature range[40].

The temperature dependent thermoelectric power factors of the *n*-type $Sc_{0.997}Mg_{0.003}N$ and $Sc_{0.987}Mg_{0.013}N$ alloy films, as well as the *p*-type $Sc_{0.967}Mg_{0.033}N$ and $Sc_{0.964}Mg_{0.036}N$ alloy films, are also presented in Fig. 2(d)-(f). Since both the heating and cooling cycles showed very similar results, transport characteristics only from the heating cycles for each of the films are presented. The Seebeck coefficient of both of the *n*-type alloy samples are very close to each other, and increased in magnitude from ~ -125 μV/K to -350 μV/K with increasing temperature from 300 K to 850 K, thus exhibiting a ~3-fold increase. In comparison to the undoped ScN, the Seebeck

coefficient of the *n*-type $Sc_{0.967}Mg_{0.033}N$ and $Sc_{0.964}Mg_{0.036}N$ alloy films are more than 2 times larger across the whole temperature range. Such an increase in Seebeck coefficient of the *n*-type alloy samples over the undoped ScN can be explained by their lower carrier concentrations, with the Fermi energy presumably being within the bandgap (see below). However, it was interesting to find that the *n*-type $Sc_{0.967}Mg_{0.033}N$ and $Sc_{0.964}Mg_{0.036}N$ alloy films exhibited very similar values of Seebeck coefficient even though their resistivity's were much different, particularly at low temperatures, with the $Sc_{0.964}Mg_{0.036}N$ alloy exhibiting 5 times higher room temperature resistivity compared to the $Sc_{0.967}Mg_{0.033}N$ alloy. These results also highlight the fact that the decreased mobility due to increased impurity scattering plays an important role in the overall Seebeck coefficient values. Similarly, the Seebeck coefficient of the *p*-type $Sc_{0.967}Mg_{0.033}N$ and $Sc_{0.964}Mg_{0.036}N$ alloy films are very close to each other, increasing from ~100 μV/K to 250 μV/K within the same temperature range. The maximum Seebeck coefficient values of the two *p*-type alloys are slightly higher than that of the *p*-type $Sc_{0.962}Mg_{0.038}N$.

The resistivity of both of the *n*-type alloy films decreased with increasing temperature from 300 K to 850 K as shown in Fig. 2(e). The resistivity of the *n*-type $Sc_{0.997}Mg_{0.003}N$ alloy film decreased by a factor of 2× from ~200 mΩ-cm to ~100 mΩ-cm, while the resistivity of the *n*-type $Sc_{0.987}Mg_{0.013}N$ thin film alloy decreased from 1000 mΩ-cm to 20 mΩ-cm, thus exhibiting a 50 times reduction. The decreases in resistivity of both films are opposite to the behavior of the undoped ScN film as a function of temperature and are a clear indication that with the increase in Mg_xN_y concentration within the ScN matrix, the Fermi level moves into the bandgap. The resistivity of the *p*-type $Sc_{1-x}Mg_xN$ thin film alloys, however, does not change appreciably with temperature as shown in the Fig. 2(e) indicating their degenerate nature. The power factors of the *n*-type $Sc_{1-x}Mg_xN$ and the *p*-type $Sc_{1-x}Mg_xN$ films are significantly smaller - in the 10^{-5} to 10^{-4} W/m-K^2 range - due to their higher resistivity values. However, the *p*-type $Sc_{0.964}Mg_{0.036}N$ alloy exhibited a high power factor (close to the best *p*-type material $Sc_{0.962}Mg_{0.038}N$) in the 500K-850K temperature range, while the *n*-type $Sc_{0.987}Mg_{0.013}N$ exhibited an increasing power factor reaching 0.6×10^{-3} W/m-K^2 at 850 K due to the decreasing electrical resistivity.

V. MODELING OF THE THERMOELECTRIC PROPERTIES

We employed the linearized Boltzmann transport equations under the relaxation time approximation to further explain the experimental observation of the thermoelectric properties[29]. The electronic band structure of undoped ScN was calculated previously[9] by the authors employing first-principles density functional theory along with a Hubbard U correction. Based on the full band electronic structure, the conduction and valence bands near the band edges were modeled as non-parabolic bands with two parameters: effective mass and non-parabolicity. Acoustic phonon deformation scattering, alloy scattering, ionized and neutral impurity scatterings were included for the electron scattering characteristics. Detailed parameters used for the modeling are shown in the methods section. Fig. 3 shows the curve-fitting results of Boltzmann transport modeling for the two best *n*-type and *p*-type materials that showed highest thermoelectric power factor. An electron concentration of 3.5×10^{20} cm^{-3} and a hole concentration of 1.3×10^{20} cm^{-3} were used for the *n*-type undoped ScN and *p*-type $Sc_{0.962}Mg_{0.038}N$ alloy film, respectively, consistent with the previous Hall measurements (Ref. 27). The slightly lower carrier concentration of the *p*-type $Sc_{0.962}Mg_{0.038}N$ alloy film explains its higher Seebeck coefficient (by ~ 50 μV/K) compared to the *n*-type undoped ScN (Fig. 3(a)) over

the entire temperature range . The modeling analysis also showed that the Fermi levels of *n*-type undoped ScN was about 0.12 eV above the conduction band edge (consistent with our previous work, Ref. 13), while the Fermi level for the *p*-type $Sc_{0.962}Mg_{0.038}N$ alloy film was ~0.2 eV below the valence band edge at 800K. The experimental observation of the resistivity increasing as a function of temperature for *n*-type undoped ScN and *p*-type $Sc_{0.962}Mg_{0.038}N$ alloy films are, therefore, consistent with the fact that their Fermi energies were within the bands, and the materials behaved like degenerate semiconductors or metals in terms of their electrical transport. Furthermore, the modeling showed that the mobility of the *p*-type $Sc_{0.962}Mg_{0.038}N$ alloy film was significantly smaller than that of the *n*-type undoped ScN (consistent with experimental observations) due to the much stronger impurity scattering imposed by extensive Mg doping, which resulted in about four times lower power factor for the *p*-type $Sc_{0.962}Mg_{0.038}N$ alloy films compared to *n*-type undoped ScN.

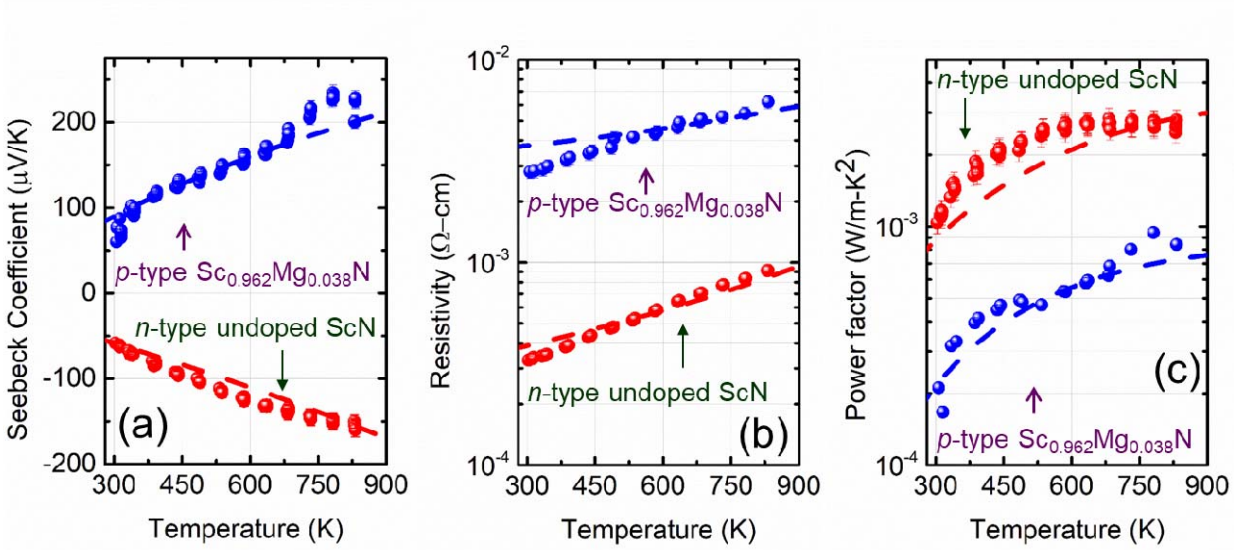

Figure 3: (a) Experimental results and Boltzmann transport based modeling fitting of the Seebeck coefficient (a), electrical resistivity (b), and power factors (c) of n-type undoped ScN and p-type $Sc_{0.962}Mg_{0.038}N$ thin film alloy are presented.

While the modeling analysis explains the observed experimental data, modeling also provides a pathway for optimizing the thermoelectric performance and electrical properties in these materials. Since the carrier concentration in ScN can be varied with changing concentrations of Mg_xN_y, we estimated the behavior of the Seebeck coefficient, electrical conductivity, thermoelectric power factor, and the position of the Fermi energy as a function of the number of carriers in both *n*-type and *p*-type carrier regimes. Consistent with expectations, both the Seebeck coefficient and electrical resistivity increased with decreasing carrier concentration (see Fig. 4). However, the extent of increase in Seebeck coefficients in our experiment was smaller than the prediction from the modeling, which highlights clearly that the decrease in mobility due to increasing Mg_xN_y concentration played an important role in suppressing the Seebeck coefficient values. It was also manifested in the fact that the carrier concentrations were already mostly optimized for achieving the highest possible power factor values as shown in Fig. 4. Further improvement of the thermoelectric power factor would, therefore, involve increasing the carrier mobility, which could be achieved by altering materials growth techniques and conditions, and by the processing of the material (such as through annealing, ion-

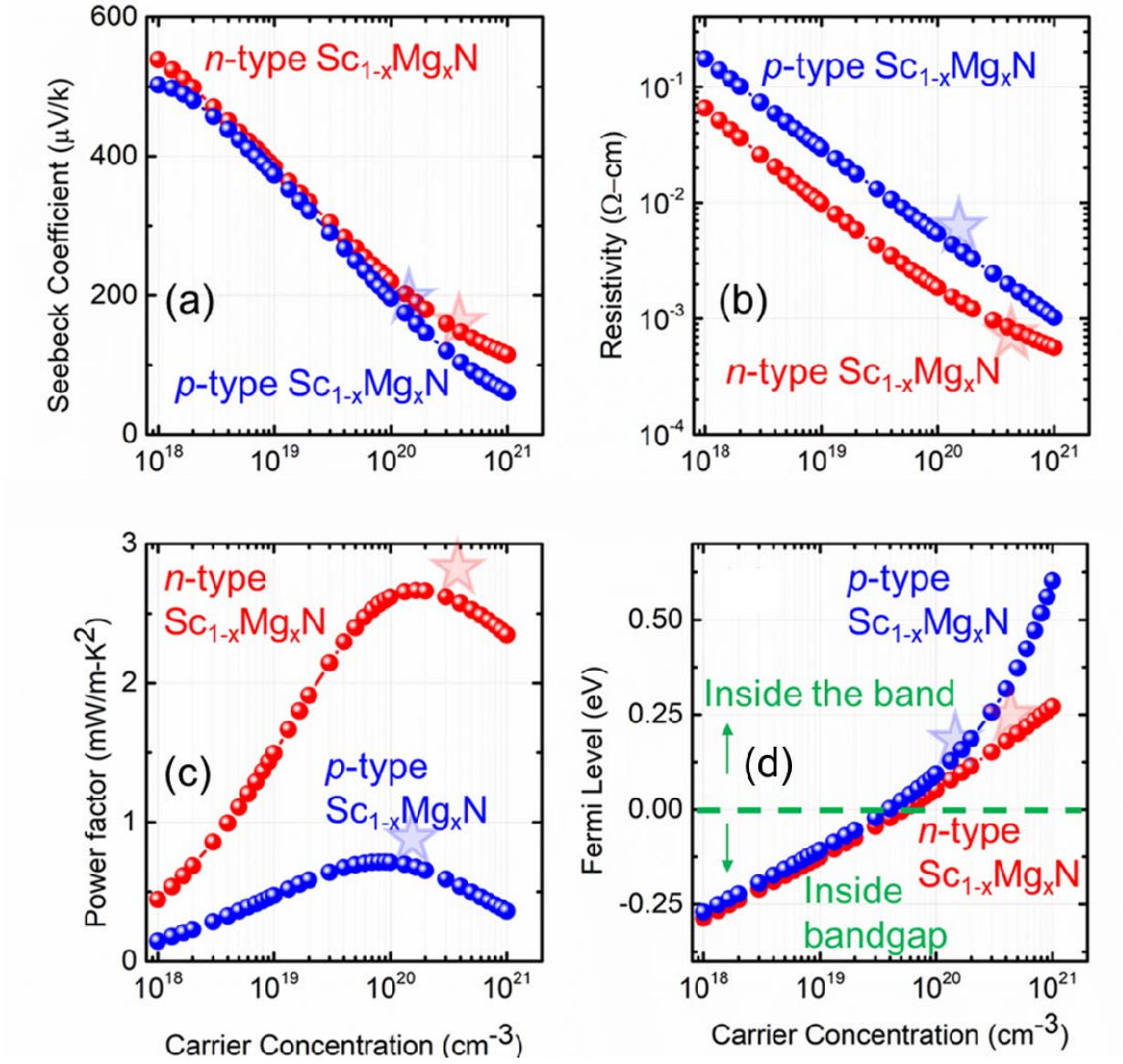

Figure 4: Theoretical calculations of the optimized Seebeck coefficient (a) and electrical resistivity (b) are presented as a function of carrier concentrations in n-type and p-type ScN films. As expected, the Seebeck coefficient and resistivity increase with decreasing carrier concentrations. The experimental values for the two best sample (n-type undoped ScN and p-type $Sc_{0.962}Mg_{0.038}N$) are plotted with star signs. Optimized Power factor (c) and Fermi energy (d) are plotted as a function of the n-type and p-type carrier concentrations. The Fermi energy positions are referenced with respect to the conduction and valence band edges. The figure shows that Power factor values at high temperatures (800K) are already optimized with respect to the carrier concentration in n-type and p-type samples.

implantation and others). Since it is known very well that for several basic electronic and optoelectronic applications, the Fermi level of ScN must be inside the bandgap, the modeling reveals that for both *n*-type and *p*-type ScN, the carrier concentration needs to be reduced below 1×10^{19} cm^{-3} and $(4\text{-}5) \times 10^{19}$ cm^{-3} at 300K and 800K respectively (see the Supplemental

Material Ref. 42). The positions of the Fermi level for *n*-type and *p*-type $Sc_xMg_{1-x}N$ thin film alloys at 800K are presented in Fig. 5 on a schematic band structure of ScN for clarity (assuming that the effective masses of the carriers doesn't change due to Mg_xN_y incorporation).

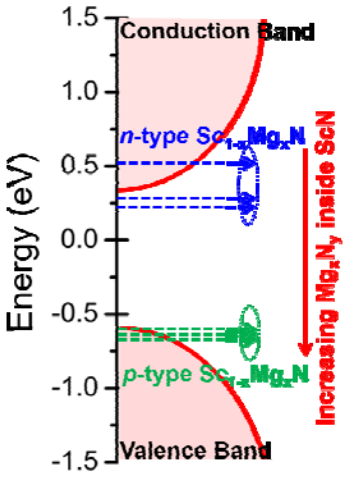

Figure 5: An electronic band diagram schematic of ScN and position of the Fermi energy in n-type and p-type samples are presented.

VI. TEMPERATURE DEPENDENT THERMAL CONDUCTIVITY

As estimates of the thermoelectric figure-of-merit (*ZT*) of the *n*-type and *p*-type $Sc_xMg_{1-x}N$ alloy films require knowledge of the temperature dependent thermal conductivities, a time domain thermoreflectance (TDTR) measurement technique was employed. A detailed description of the experimental technique is presented in the methods section. Representative experimental ratio curves along with the fittings are shown in Fig. 6(b) for *n*-type undoped ScN at different temperatures. Thermal conductivity of the *n*-type undoped ScN and *p*-type $Sc_{0.962}Mg_{0.038}N$ thin film alloy (see Fig. 6(a)) decreased with increasing temperature, suggestive of high-temperature Umklapp phonon scattering behavior. Surprisingly, the room temperature thermal conductivity of *p*-type $Sc_{0.962}Mg_{0.038}N$ (κ =14.2 W/m-K) was found to be slightly higher than that of the *n*-type undoped ScN (κ =13.6 W/m-K). Given that the *p*-type $Sc_{0.962}Mg_{0.038}N$ incorporated 3.8 atomic percentage of Mg_xN_y within the ScN matrix, the small increase in thermal conductivity of the alloy could be due to changes in crystal quality (sound velocity) or due to the dominance of alloy phonon scattering in *p*-type $Sc_{0.962}Mg_{0.038}N$, which would partially suppress an otherwise sharp decrease in thermal conductivity due to Umklapp scattering. While further work on low-temperature thermal conductivity measurements will be necessary to address this issue, a detailed description of possible reasoning is presented in the Supplemental Material section Ref. 42.

The decrease of thermal conductivity in *n*-type undoped ScN was much faster in comparison to the *p*-type $Sc_{0.962}Mg_{0.038}N$ thin film alloy with increasing temperatures, as shown in Fig. 4(a). Fittings of the temperature dependent thermal conductivity of the *n*-type undoped ScN and *p*-type $Sc_{0.962}Mg_{0.038}N$ thin film alloy with an Umklapp scattering model ($\kappa = AT^{\alpha}$, where κ, T, α,

A are the thermal conductivity, absolute temperature, Umklapp exponent and a constant, respectively) yielded values of -0.85 and -0.57, respectively. This is not surprising, given the fact that semiconductor alloys typically exhibit much smaller Umklapp scattering exponents in comparison to undoped semiconductors[43,44]. The electronic thermal conductivity of the *p*-type

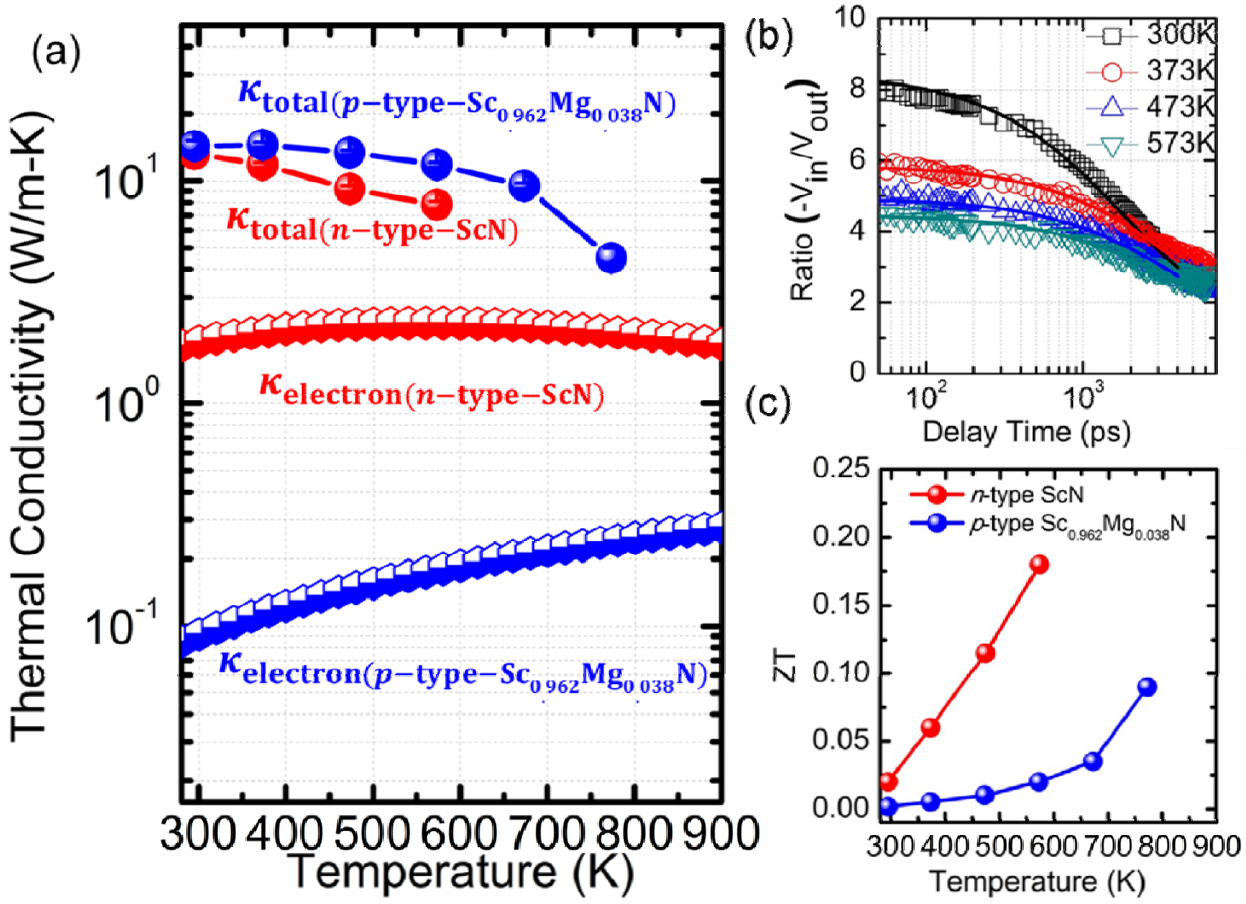

Figure 6: (a) Total thermal conductivity along with the electronic contributions to the thermal conductivity of n-type undoped ScN and a p-type $Sc_{0.962}Mg_{0.038}N$ thin film alloy are presented in the 300K - 850K temperature range. The thermal conductivities of both materials decrease with increasing temperatures due to Umklapp scattering. (b) The experimental ratio curves and data fitting in TDTR measurements are presented at four different temperatures for n-type undoped ScN. (c) Thermoelectric figure-of-merit (ZT) of n-type undoped ScN and p-type $Sc_{0.962}Mg_{0.038}N$ thin film alloy (exhibiting maximum values within their class) are presented. ZT of n-type undoped ScN has a maximum value of 0.2 at 600K, while the p-type $Sc_{0.962}Mg_{0.038}N$ thin film alloy exhibits a ZT of 0.1 at 800K.

$Sc_{0.962}Mg_{0.038}N$ thin film alloy (estimated from the electrical conductivity measurements with the assumption of the validity of the Wiedemann-Franz's law with Lorentz number obtained from Boltzmann transport analysis) was about 10 times smaller than the value for *n*-type undoped ScN due to its higher resistivity. The overall values of the thermal conductivity for both the *n*-type and *p*-type materials were, however, quite large (12-15 W/m-K) at room temperature, and 7-9 W/m-K at higher temperatures, which resulted in a low ZT value of 0.05-0.2 in these materials (see Fig. 6(c)). A maximum *ZT* of 0.2 was achieved in *n*-type undoped ScN at 600K, which is, however, significantly higher than any other III-V nitride materials. Significant efforts have been made in recent years to reduce the thermal conductivity of ScN with the development of ScCrN

and ScNbN solid-solution alloys, which exhibit reduced thermal conductivities[45,46]. However, like the challenges encountered in most other thermoelectric materials systems, the reduction in thermal conductivity must be attained without reducing the power factor, for achieving higher *figure-of-merit (ZT)*. In this regard, incorporation of nanoparticles, phase separation, a small amount of heavy element inclusion, and other approaches may be explored for $Sc_{1-x}Mg_xN$ thin-film alloys.

VII. CONCLUSION

In conclusion, thermoelectric properties of *n*-type and *p*-type $Sc_xMg_{1-x}N$ thin film alloys were investigated using a combination of temperature-dependent Seebeck coefficient, electrical conductivity, and thermal conductivity measurements, and Boltzmann transport theory-based analyses of the transport properties. Both the *n*-type undoped ScN and the highly doped *p*-type $Sc_{0.962}Mg_{0.038}N$ thin film alloy exhibited large thermoelectric power factors of $\sim 3.0 \times 10^{-3}$ W/m-K^2 and $\sim 0.8 \times 10^{-3}$ W/m-K^2, respectively, at higher temperatures (600-850K). The modeling analysis revealed that the Fermi level in the alloy films moved all the way from inside the conduction band for sputter-deposited *n*-type undoped ScN to inside the valence band in a highly doped *p*-type $Sc_xMg_{1-x}N$ thin film alloy. Modeling also revealed that the doping ranges explored experimentally coincided with nearly optimal doping levels for maximizing the power factor. Despite the large power factors, the thermoelectric *figures-of-merit* of the materials were rather low due to their high thermal conductivities. Further experiments on nanoparticle inclusion, phase separation, and other strategies will, therefore, have to be used for harnessing $Sc_{1-x}Mg_xN$'s potential for thermoelectric devices.

IV. ACKNOWLEDGEMENTS

B.S. and T.D.S. acknowledge financial support by the National Science Foundation and US Department of Energy (CBET-1048616). M.M.G. acknowledges financial support from ERC Starting grant NanoTEC 240497, and the INFANTE project 201550E072. J.A.P.T. acknowledges the FPI from the project PHOMENTA (MAT2011-27911).

References

1. C. J. Vineis, A. Shakouri, A. Majumdar, and M. G. Kanatzidis, Adv. Matt. **22**, 3970 (2010).
2. A. Majumdar, *Science, **303**, 5659, (2004).*
3. J. R. Sootsman, D. Y. Chung, and M. G. Kanatzidis, *Angewandte Chemie, **48**, 8616, (2009).*
4. F. J. DiSalvo, *Science, **285**, 5428, (1999).*
5. G. J. Snyder, M. Soto, R. Alley, D. Koester, and B. Conner, *22nd IEEE SEMI-THERM Symposium, 9005043, **135**, (2006).*
6. L. Zhao, S. Lo, Y. Zhnag, H. Sun, G. Tan, C. Uher, C. Wolverton, V. P. Dravid, M. G. Kanatzidis, *Nature, **508**, 373, (2014).*
7. K. Biswas, J. He, I. D. Blum, C. Wu, T. P. Hogan, D. N. Seidman, V. P. Dravid, M. G. Kanatzidis*, Nature, 489, 414, (2012).*
8. B. Poudel, Q. Hao, Y. Ma, Y. Lan, A. Minnich, B. Yu, X. Yan, D. Wang, A. Muto, D. Vashaee, X. Chen, J. Liu, M. S. Dresselhaus, G. Chen and Z. Ren, *Science, 320, 634, (2008).*
9. B. Saha, J. Acharya, T. D. Sands and U. V. Waghmare, *J. Appl. Phys. **107**, 033715 (2010).*
10. B. Saha, G. Naik, V. Drachev, A. Boltasseva, E. E. Marinero, and T. D. Sands, *J. Appl. Phys., **114**, 063519 (2013).*
11. D. Gall, I. Petrov, N. Hellgren, L. Hultman, J. E. Sundgren, and J. E. Green, *J. Appl. Phys. **84**, 6034 (1998).*
12. H. A. Al-Brithen, A. Smith, and D. Gall, *Phys. Rev. B **70**, 045303 (2004)*.
13. J. P. Dismukes, W. M. Yim, and V. S. Ban, *Journal of Crystal Growth 13/14, 365, (1972).*
14. G. Harbeke, E. Meier, and J. P. Dismukes, *Optics Communications, Vol. 4, Number 5, 335, (1972).*
15. M. A. Moram, Z. H. Barber, C. J. Humphreys, T. B. Joyce and P. R. Chalker, *J. Appl. Phys. 100, 023514, (2006).*
16. P. V. Burmistrova, J. Maassen, T. Favaloro, B. Saha, S. Salamat, Y. R. Koh, M. S. Lundstrom, A. Shakouri, and T. D. Sands, *J. Appl. Phys. **113**, 153704 (2013).*
17. S. Kerdsongpanya, N. van Nong, N. Pryds, A. Zukauskaite, J. Jensen, J. Birch, J. Lu, L. Hultman, G. Wingqvist, and P. Eklund, *Appl. Phys. Lett. **99**, 232113 (2011).*
18. P. V. Burmistrova, D. N. Zakharov, T. Favaloro, A. Mohammed, E. A. Stach, A. Shakouri, and T. D. Sands, *Journal of Materials Research, 30, 626-634, (2015).*
19. M. Garbrecht, J. L. Schroeder, L. Hultman, J. Birch, B. Saha, and T. D. Sands, *J. Mater. Sci.*, ***51**, 8250 (2016)*.
20. M. Garbrecht, B. Saha, J. L. Schroeder, L. Hultman, and T. D. Sands, *Sci. Rep. 7, 46092; (2017).*
21. M. Zebarjadi, Z. Bian, R. Singh, A. Shakouri, R. Wortman, V. Rawat, and T. Sands, *Journal of Electronic Materials, 38, 960-963, (2009).*
22. V. Rawat, Y. K. Koh, D. G. Cahill and T. D. Sands, *J. Appl. Phys. 105, 024909, (2009).*
23. M. A. Moram, Y. Zhang, M. J. Kappers, Z. H. Barber, and C. J. Humphreys, *Appl. Phys. Lett. **91**, 152101 (2007).*
24. M. A. Moram, M. J. Kappers, and C. J. Humphreys, *Phys. Status Solidi C 7, 1778 (2010).*
25. C. Stampfl, W. Mannstadt, R. Asahi, and A. J. Freeman, *Phys. Rev. B **63**, 155106 (2001).*
26. S. Adachi, Properties of Semiconductor Alloys: Group-IV, III–V and II–VI, Semiconductors *(John Wiley & Sons, Chichester, 2009).*

27. R. P. Deng, B. Ozsdolay, P.Y. Zheng, S. V. Khare, and D. Gall. *Phys. Rev. B. 90, 045104 (2015).*
28. W. R. L. Lambrecht, *Phys. Rev. B* ***62****, 13538 (2000)*.
29. B. Saha, Y. R. Koh, J. Comparan, S. Sadasivam, J. L. Schroeder, M. Garbrecht, A. Mohammed, J. Birch, T. S. Fisher, A. Shakouri, T. D. Sands, *Phys. Rev. B,* ***93****, 045311 (2016).*
30. B. Saha, G. V. Naik, S. Saber, E. Stach, V. M. Shalaev, A. Boltasseva, and T. D. Sands, *Phys. Rev. B, 90, 125420, (2014).*
31. F. Tasnádi, B. Alling, C. Höglund, G. Wingqvist, J. Birch, L. Hultman, and I. A. Abrikosov, *Phys. Rev. Lett.* ***104****, 137601 (2010).*
32. H. L. Gao, T. J. Zhu, H. Wang, Z. F. Ren, and X. B. Zhao, *J. Phys. D: Appl. Phys. 45, 185303 (2012).*
33. H. Takiguchi, A. Matoba, K. Sasaki, Y. Okamoto, H. Miyazaki, and J. Morimoto, *Mater. Trans. 51, 878 (2010).*
34. S. Kerdsongpanya, B. Alling, and P. Eklund, *Phys. Rev. B. 86, 194140 (2012).*
35. M. G. Moreno-Armenta and G. Soto, *Comput. Mater. Sci. 40, 275 (2007).*
36. R. Deng, Y. P. Zheng, and D. Gall, J. Appl. Phys. 118, 015706, (2015).
37. B. Saha, M. Garbrecht, J. Anders, Y. R. Koh, L. Hultman, M. M. Gonzalez, A. Shakouri and T. D. Sands, *Appl. Phys. Lett, 110, 252104, (2017).*
38. D. G. Cahill, *Rev. Sci. Instrum.* ***75****, 5119 (2004).*
39. S. Dilhaire, G. Pernot, G. Calbris, J. M. Rampnoux, and S. Grauby, *J. Appl. Phys.* ***110****, 114314 (2011).*
40. A. M. Dehkordi, M. Zebarjadi, H. He, and T. M. Tritt, *Materials Science and Engineering, R97, 1-22, (2015).*
41. J. Bahk, Z. Bian, and A. Shakouri, *Phys. Rev. B. 89, 075204, (2014).*
42. See supplementary materials at () for the details about the (a) fermi Level as a function of carrier concentration, and (b) Umklapp fittings and possible explanation for high thermal conductivity in alloy films.
43. G. A. Slack, R. A. Tanzilli, R. O. Pohl, and J. W. Vandersande, *J. Phys. Chem. Solids* **48, 7** 641-647 (1987).
44. M. D. Kamatagi, N. S. Sankeshwar, and B. G. Mulimani, Diamond and Related Materials, 16, 98 (2007).
45. N. Tureson, N. V. Nong, D. Fournier, N. Singh, S. Acharya, S. Schmidt, L. Belliard, A. Soni, A. Febvrier, P. Eklund, *J. Appl. Phys. 122, 025116, 92017).*
46. S. Kerdsongpanya, B. Sun, F. Eriksson, J. Jensen, J. Lu, Y. K. Koh, N. V. Nong, B. Balke, B. Alling, P. Eklund, *J. Appl. Phys.120, 215103 (2016).*